



ELSEVIER

Contents lists available at ScienceDirect

## Surface &amp; Coatings Technology

journal homepage: [www.elsevier.com/locate/surfcoat](http://www.elsevier.com/locate/surfcoat)

# Influence of overstoichiometric boron and titanium addition on the properties of RF magnetron sputtered tungsten borides

Tomasz Moscicki<sup>a,\*</sup>, Rafal Psiuk<sup>a</sup>, Hanna Słomińska<sup>a</sup>, Neonila Levintant-Zayonts<sup>a</sup>, Dariusz Garbiec<sup>b</sup>, Marcin Pisarek<sup>c</sup>, Piotr Bazarnik<sup>d</sup>, Szymon Nosewicz<sup>a</sup>, Justyna Chrzanowska-Giżyńska<sup>a</sup>

<sup>a</sup> Institute of Fundamental Technological Research, Polish Academy of Sciences, Pawlowskiego 5B, 02-106 Warsaw, Poland

<sup>b</sup> Lukaszewicz Research Network - Metal Forming Institute, Jana Pawła II 14, 61-139 Poznan, Poland

<sup>c</sup> Institute of Physical Chemistry, Polish Academy of Sciences, Kasprzaka 44/52, 01-224 Warsaw, Poland

<sup>d</sup> Faculty of Material Science and Engineering of Warsaw University of Technology, Wołoska 141, 02-507 Warsaw, Poland

## ARTICLE INFO

## Keywords:

Superhard films  
Ternary tungsten borides  
RF magnetron sputtering  
Wear resistance  
Corrosion

## ABSTRACT

In this work, (W,Ti)B<sub>2</sub> films with different stoichiometric ratio Ti/W deposited on silicon and 304 stainless steel by radio frequency magnetron sputtering are presented. The coatings were deposited from plasma spark sintered targets obtained from the mixture of pure boron, tungsten and titanium powders. It is shown that during plasma spark sintering process using overstoichiometric boron and a low content of titanium change the WB<sub>2</sub> to WB<sub>4</sub> phase with almost no secondary phases. Subsequently, the impact of titanium content on the films properties is investigated systematically, including the chemical and phase composition, crystalline structure, surface and cross-section morphology. Simultaneously, nano-indentation test and ball-on-disk tribometry are performed to analyse the hardness and tribological properties of the films. It is shown that deposited films with titanium content of 3.6 and 5.5 at.% are formed in the zone T of the Thornton's Structural Zone Model. In opposite to α-WB<sub>2</sub> magnetron sputtered coatings they are more flexible and hard nanocomposite coatings. The results show that the addition of titanium is apparently changing the film structure from nanocrystalline columnar to amorphous, very dense and compact structure with the addition of TiB<sub>2</sub> phase. That films are simultaneously hard ( $H > 37.5$  GPa), have high hardness to effective Young's modulus ratio values ( $H/E^* > 0.1$ ) and elastic recovery ( $W_e > 60\%$ ) appropriate for tough and resistant to cracking materials. The presented (W,Ti)B<sub>2</sub> films exhibit also tribological and corrosion properties better than unalloyed coatings.

## 1. Introduction

The development of many modern advanced technologies requires creating new and improving known materials feature high performance in the context of constantly increasing production requirements. Designing materials with given properties can be successfully solved by multi-element coating methods using ion-plasma technologies, which are successfully used for protective coatings composed of nitrides, carbides and borides of transition metals (TM). While the use of hard-wearing and corrosion-resistant materials based on nitrides and carbides has found its place in production, the industrial application of thin films based on borides is rather limited and still under investigation [1–4].

Theoretical [3,5–9] and experimental studies [10–13] indicate that tungsten borides demonstrate many remarkable mechanical, thermal

and chemical properties. Even as a thin films, due to their super-hardness, incompressibility, low friction coefficient and good thermal stability tungsten borides can have many potential applications including materials for tools and abrasives. Previous research shows that it is possible to deposit this material in different phases depending on the selected method and setting parameters. Yang et al. [14,15] prepared bcc-W coating doped by B via magnetron co-sputtering W and B targets. The coatings including W, α-W(B) supersaturated solid solution and W<sub>2</sub>B were synthesized. The incorporation of 6.3 at.% B in W film remarkably improve its hardness from  $14.1 \pm 0.93$  GPa to  $28.1 \pm 0.79$  GPa and deposited films have low friction coefficient (~0.18). Due to higher crack formation threshold induced by finer grains, and the higher H/E\* (> 0.1) improving crack resistance W(B) films exhibits enhanced toughness. W<sub>2</sub>B coatings deposited with higher concentration of boron possess intrinsically low hardness (~20 GPa).

\* Corresponding author.

E-mail address: [tmosc@ippt.pan.pl](mailto:tmosc@ippt.pan.pl) (T. Moscicki).

<https://doi.org/10.1016/j.surfcoat.2020.125689>

Received 23 January 2020; Received in revised form 23 March 2020; Accepted 24 March 2020

Available online 25 March 2020

0257-8972/ © 2020 The Authors. Published by Elsevier B.V. This is an open access article under the CC BY license (<http://creativecommons.org/licenses/by/4.0/>).

The  $W_2B$  films were also deposited using radio frequency (RF) magnetron sputtering method from single W–B target with 27 at.% B by Willer et al. [16]. Deposited films are amorphous and very stable. Annealing at 880 °C enables to identify the crystalline phases of tungsten and  $W_2B$ . Because of high crystallization temperature, those coatings are suggested as candidate for an amorphous diffusion barrier. Taking in account the W–B phase diagram and enthalpies of W–B compounds formation, the next deposited stable phase with increasing boron concentration should be  $\alpha$ -WB with the lowest  $\Delta E = -0.375$  eV/atom [9]. It is possible to deposit this phase by RF magnetron sputtering from the  $WB_{2.5}$  target on heated (320–550 °C) substrate [17,18]. The deposited films are crystalline with highly oriented columnar structure. Such coatings possess a high hardness 45 GPa, Young's modulus about 525 GPa, a smooth surface with a mean roughness  $R_a = 0.002$   $\mu\text{m}$  and a good adhesion. The wear resistance of the coating is  $2.7 \cdot 10^{-6}$   $\text{mm}^3 \text{N}^{-1} \text{m}^{-1}$ . In comparison with the uncoated stainless steel substrate, the wear rate decreases almost 25 times. Additionally, films are thermally stable to 250 °C in air and does not change the surface appearance and its chemical and phase composition during annealing in argon to 1000 °C. Sobol et al. [19,20] during DC-magnetron sputtering of a  $WB_2$  target (hexagonal crystal lattice) obtained the  $\beta$ -WB phase with an orthorhombic crystal lattice and a B/W atoms ratio of about 1.19. The films deposited at 700 °C possess lower hardness ( $26.7 \pm 0.5$  GPa) and elastic modulus ( $376 \pm 7$  GPa) than low temperature MoB-type tungsten boride presented in [17]. The increase of the DC power and applying the appropriate bias voltage during DC-MS of  $WB_2$  target leads to deposition of  $AlB_2$  - type  $WB_2$  coatings [21–24].  $AlB_2$  - type  $WB_2$  is metastable phase and firstly was reported by Woods et al. [25] in 1966. In this case, the thin film is prepared by resistively heating an amorphous boron wire in a mixed atmosphere of  $WCl_6$  and Ar at 800 °C. Its crystal structure is assumed to crystallize in an  $AlB_2$ -type structure (No.191, P6/mmm,  $a = 3.02$  Å,  $c = 3.05$  Å). Prepared by this method film is porous and cannot be used for further investigations of its basic properties. The  $AlB_2$ -type  $WB_2$  coatings deposited by the DC magnetron sputtering method were also extensively investigated due to influence of deposition parameters on properties of films by Liu et al. [21–24]. It is shown that coatings are dense and uniform with columnar structure. Because of the superhardness (43.2 GPa), steady-state friction coefficient (0.23) and wear rate about  $6.5 \cdot 10^{-6}$   $\text{mm}^3 \text{N}^{-1} \text{m}^{-1}$  the  $AlB_2$ -type  $WB_2$  coatings have high potential application in industry. Additionally, Liu and coworkers [26] showed that the mechanical, tribological and corrosion properties of the  $WB_2$  films can be improved by doping a small amount of nitrogen when  $P_{N_2} \leq 0.006$  Pa. Greater nitrogen content leads to properties deterioration due to the increasing content of soft BN phase and the enhanced compressive stress. For N-doping (5.6 at.%) of  $WB_2$  films deposited on Si wafers, the thermal stability of the  $AlB_2$  - type  $WB_2$  phase is improved greatly from 700 °C to 1000 °C due to the stabilization effect of a-BN. Similar effect is possible by tantalum alloying [1,27]. The results clearly reveal the enormous potential of  $\alpha$ - $WB_2$ -based coatings in combining high strength with high fracture toughness  $3.8 \pm 0.5$   $\text{MPa m}^{1/2}$  ( $W_{0.93}Ta_{0.07}B_{1.76}$ ) [1]. Experimental and theoretical studies show that  $WB_4$  phase has great application potential as superhard, incompressible material with high thermal oxidation temperature [4,10]. Until now there are a few reports about pulsed laser deposition (PLD) [28–30] or chemical deposition [31,32] of this

material. In the case of PLD deposition films are superhard but have high roughness. It is also possible to deposit a single  $WB_4$  phase by applying the confined-plume chemical deposition (CPCD) but there is lack of information about thermal and mechanical properties of obtained layers [32]. The problem with synthesizing of  $WB_4$  phase in lower temperatures is necessity of using excess boron with W:B ratio at least of 1:9 [10]. This problem can be solved by adding of a second metal, for example thallium [10], then  $WB_4$  can be stabilized with a nearly stoichiometric amount of boron (4.5) with no secondary phases. The addition of titanium to  $WB_x$  coatings were carried out earlier [19,20,33–36], however, the content of boron in the target did not exceed 2.5. Sputter deposited  $W_xTi_{1-x}B_{2-z}$  thin films are shown to crystallize in the columnar  $AlB_2$  structure type. Also hardness for samples of  $WB_2$ -TiB<sub>2</sub> system is noticeably higher than for coatings obtained by sputtering with poor  $WB_2$  content [19,36]. Adding small amount of titanium can change phase composition from  $\beta$ -WB to  $AlB_2$ -type  $WB_2$  [19,33]. Deposited coatings are thermally stable up to 800 °C for low Ti content and up to 1000 °C for Ti concentration > 37% at [36]. Chrzanoska et al. [37] proposed combined magnetron sputtering and pulsed laser deposition technique for alloying WB films by titanium. By changing the laser fluence at the surface of titanium target it is possible to control the ablation rate and hence the dopant content. At titanium content of 5.5 at.% the hardness and Young's modulus of coatings are very high and do not differ from un-alloyed WB coating presented in [17]. However, the titanium alloying results in changing initial  $\alpha$ -WB structure to the mixed  $\alpha$ -WB and  $AlB_2$ -type  $WB_2$  structure with some admixture of  $W_2B$ . Until now the  $WB_x$  films (where  $x > 1$ ) are not deposited by RF magnetron sputtering. Particles possess higher energy then during DC magnetron sputtering which can affect overstoichiometric content of boron [19].

In this work we investigated the influence of overstoichiometric boron and titanium addition on the properties of spark plasma sintered (SPS) and RF magnetron sputtered tungsten borides materials. The effects of Ti addition on the film structure, phase composition, mechanical and tribological properties were investigated systematically. We proposed method of obtaining very hard  $\alpha$ -(W,Ti) $B_2$  thin films with the increased crack resistance and good tribological performance. Due to the potential application of (W,Ti) $B_2$  films in high humidity or corrosive environments, the corrosion behavior of the films was studied.

## 2. Material and methods

### 2.1. Spark plasma sintering (SPS)

The spark plasma sintering process was performed using a HP D 25/3 (FCT Systeme GmbH) furnace. Targets were fabricated from boron (~625 mesh, 99.7% purity, Sigma Aldrich), tungsten (12  $\mu\text{m}$ , 99.9% purity, Sigma Aldrich) and titanium (45  $\mu\text{m}$ , 99.98% purity, Sigma Aldrich) which were sintered in various molar ratio. The sintering parameters and molar ratio of the elements due to formula  $W_{1-x}Ti_xB_y$  are shown in Table 1. Purchased elements were milled and ultrasonically mixed. For this purpose, tools made from 2333 graphite were used (MERSEN d. Carbone Lorraine). The loading chamber in the graphite tools unit was filled with the powder mixture. For experimental reasons, Papyex N998 graphite film (MERSEN d. Carbone Lorraine) was placed between the powder mixture and the die and punches. Such

**Table 1**  
Parameters of sintering.

	W (1-x)	Ti (x)	B (y)	Temperature [°C]	Holding time [min]	Compacting pressure [MPa]	Heating rate [°C/min]
1	1	0	4.5	1600	2.5	50	50
2	0.92	0.08					
3	0.84	0.16					
4	0.76	0.24					

prepared tools unit were then placed in the sintering chamber of the HP D 25-3 furnace to perform the sintering process.

The cylindrical samples with the diameter of 1" (25.4 mm) and 3 mm thickness were produced.

## 2.2. Magnetron sputtering

W-Ti-B films were deposited by RF magnetron sputtering on Si(100) and 304 stainless steels (SS 304) plates. Before sputtering metallic substrates were polished to an average roughness  $R_a$  of about 0.002  $\mu\text{m}$ . The substrates were cleaned with subsequent rinses in acetone, alcohol and deionized water. W-Ti-B layers deposited on Si(100) substrates were used for structural, chemical and mechanical analysis while those on SS 304 were used for tribological and corrosion tests. Each of the substrates was mounted on a rotating substrate holder and heated to 520 °C. Heating was performed for better layer-to-substrate adhesion [17].

The deposition was performed in a vacuum chamber pumped to residual pressure of  $10^{-3}$  Pa, and then filled with argon to a working pressure of 0.9 Pa. The argon flow was 19 mL/min and it was adjusted with a mass flow controller. The water-cooled W-Ti-B targets were mounted in the 1" magnetron source (Kurt J. Lesker TORUS Magnetron Sputtering Cathode) and positioned at a distance of 40 mm from the substrate. The RF sputtering power was 50 W. The bias potential on the substrate was floating. Pre-sputtering of the target was carried out for 5 min prior to each deposition. Then, the substrate holder was positioned next to the magnetron. The deposition time was about 45 min. The deposition conditions were chosen due to the best mechanical and tribological properties of films presented in [18].

## 2.3. Characterisation

The crystal structure and phase composition of the targets were examined by X-Ray diffraction (XRD) using Bruker D8 Discover (Cu radiation,  $\lambda = 1.5418 \text{ \AA}$ ). In the case of deposited layers, measurements were taken in the  $2\theta$  scan mode, with the source fixed at 8° position. In this configuration, it was possible to avoid a signal from the substrate, while maintaining high intensity of the signal originating primarily from the coating.

The surface quality was analysed using a scanning electron microscopy (SEM JSM6010PLUS/LV JEOL). BSE (backscattered electrons) mod was used to detect contrast between areas with different chemical compositions in targets. In addition, an Energy Dispersive X-ray Spectroscopy (EDS) microanalysis was used to study the elemental distribution of B, Ti and W in the investigated samples. During EDS measurements an accelerating voltage of 5 kV was used, according to ref. [38]. Due to problems with boron measurement and subsequently determining its quantity in combination with other, especially heavy elements, before measurement the EDS spectrometer was calibrated on the base of polished  $\text{W}_2\text{B}_5$  commercial standard (TYR material, 99.9% purity).

The chemical state, in particular the detection of binding energy of titanium, tungsten and boron compounds was carried out by X-Ray Photoelectron Spectroscopy (XPS) using a Microlab 350 spectrometer (Thermo Electron). Prior to measurement, the samples were sputtered by Ar + ions. The following ion etching parameters were used: ion beam energy 2 keV, beam current 1.3  $\mu\text{A}$ , time 300 s, size of sputtering area  $6 \times 6 \text{ mm}$ . The XPS spectra were acquired using Al K $\alpha$  ( $h\nu = 1486.6 \text{ eV}$ ) radiation. The survey spectra were recorded in the electron binding energy from 1350 to 0 eV with 1.0 eV step. The high resolution (HR-XPS) spectra were collected in a narrow range of binding energy with 0.1 eV step and with pass energy of 40 eV. The intensity of XPS signal was determined by subtracting Shirley background. XPS spectra were deconvoluted using the Gauss/Lorentz asymmetric mixed function and the measured binding energies were corrected based on the C1s energy at 285.0 eV after ion sputtering

process. Due to the limitations of the XPS [39,40] method, chemical composition measurements were performed to verify EDS results only.

Detailed microstructural observations were performed using a Cs-corrected High-Resolution Scanning Transmission Electron Microscope (STEM) (Hitachi HD-2700). The STEM images were taken in bright-field (BF) and selective area electron diffraction (SAED) mode. In SAED mode the patterns were acquired by inserting a 250 nm of aperture. The samples for STEM observations were prepared using a focused ion beam (FIB) technique with a Hitachi NB5000 microscope. The coatings thickness was estimated base on TEM images of film cross-section.

The hardness of the selected layers was measured using Ultra-low Load Indentation system (CSM Instruments). For all measurements, a diamond Berkovich-shaped indenter was used. At least 8 indentations were made for each sample. The Young's modulus and hardness were specified using the Oliver-Pharr method [41]. The elastic recovery  $W_e$  was estimated on the basis of load-displacement curve. The elastic recovery  $W_{e_s}$  corresponds to the area ratio in the indentation hysteresis loop, i.e., the ratio of the recovered area and the total area [42].

Dry-sliding-wear tests were performed on a tribo-tester using ball-on-plate configuration in a reciprocating motion style. The test was conducted under applied normal loads of 0.3 N and 0.5 N using  $\text{Al}_2\text{O}_3$  ball with a diameter of 6 mm and at 1 h of sliding time, such as a similar to wear test condition in [18]. The trace length after wear was 3 mm. Three to five wear tests were conducted for each condition in order to obtain statistically valid results. To determine the wear resistance of the W-Ti-B coatings, all grooves after wear test (cross-section profiles of wear track) were measured by scanning profilometry technique (Hommel Tester T8000). The average width and depth of the groove were calculated from three taken profiles from each groove after wear. A detailed description of the wear test device and measuring the effects of wear were presented in [43].

The effect of titanium on the corrosion resistance of deposited films was investigated in the electrochemical corrosion tests – impedance spectroscopy and polarization. Samples were installed in a corrosion cell where coatings were exposed at 0.5 M NaCl solution. In the test, a standard saturated calomel electrode (SCE) as a reference electrode and platinum as a counter electrode were used. The contact area in all cases was 1  $\text{cm}^2$  and the tests were carried out at ambient temperature ( $20 \pm 5 \text{ }^\circ\text{C}$ ). The stabilization of corrosion potential took 1 h. After impedance tests, potential were decreased for 0.2 V and polarization tests were performed. Results of spectroscopy impedance are shown on Nyquist (real vs. imaginary impedance) and Bode plots (phase and impedance modulus vs. frequency) while polarization was analysed on the basis of the Tafel lines (current density vs. corrosion potential) [44]. In electrochemical spectroscopy impedance section only comparison between coating containing Ti was presented. Stainless steel and pure W–B coating results show correlation typical for bulk materials and adding them to presented plots would make them unclear and difficult to interpret.

## 3. Results and discussion

### 3.1. W-Ti-B targets

The analysis of X-ray diffractograms was used to determine phase composition of targets. As seen in Fig. 1. the phase composition changed from 91.8% of  $\text{WB}_2$  ( $\text{P}_{63/\text{mmc}}$ ) + 8.2%  $\text{WB}_4$  ( $\text{P}_{63/\text{mmc}}$ ) [30] to 4.6%  $\text{WB}_2$  (JCPDS 01-073-1244) + 95.4%  $\text{WB}_4$  (JCPDS 00-019-1373) for 0 and 8 at.% Ti, respectively. The exact structure of tungsten borides is still a matter of vigorous debate in the literature. The theoretical calculations show that  $\text{WB}_4$  may be in fact the defect-containing  $\text{WB}_3$  [9,45,46]. However, Kaner et al. [47] had unambiguously proved the existence of superhard  $\text{WB}_4$  phase by combined refinement of X-ray powder, X-ray single crystal, and neutron time-of-flight power diffraction data. Moreover, they demonstrate that the crystal structure of  $\text{WB}_4$  not only contains partially filled tungsten sites (one-third of W atoms

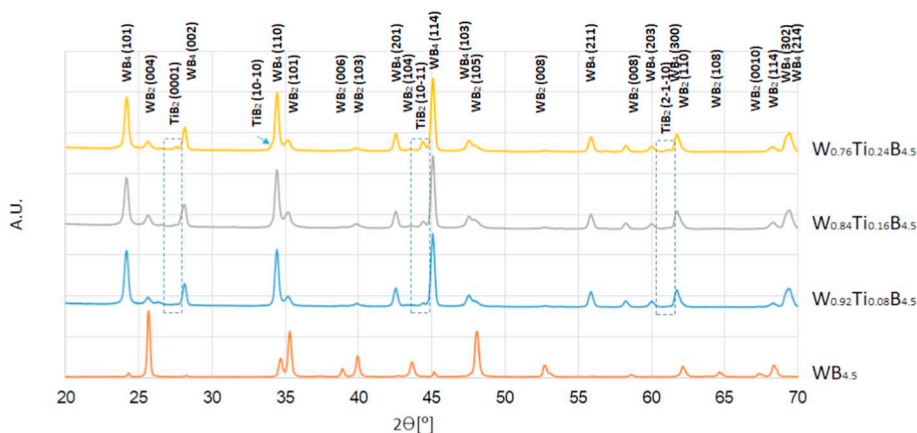


Fig. 1. XRD patterns of  $W_{1-x}Ti_xB_{4.5}$  targets with  $x = 0-24$  at.% titanium. Dashed lines indicate growing content of  $TiB_2$  phase.

are systematically absent) but also boron trimer sites [47]. Therefore, in the rest of the manuscript the designation  $WB_4$  will be used. An increase in the content of  $WB_4$  phase was possible by providing an excess of boron to stabilize the compound or adding another transition metal [10]. For example a nearly single phase ( $WB_4$ ) compound was successfully stabilized with tantalum and prepared with a nearly stoichiometric amount of boron (4.5) as  $W_{0.668}Ta_{0.332}B_{4.5}$  [10]. In the case of titanium Akopov et al. showed Ti is soluble in  $WB_4$  below 20 at.% but at higher concentrations, a secondary phase,  $TiB_2$  (JCPDS 01-075-0967) appears [48]. Additionally, the excess of boron is still needed. In our case W-Ti-B compound is stabilized with titanium and prepared with a nearly stoichiometric amount of boron (4.5). Presented in the Fig. 1 XRD spectra of targets are similar to each other. However, the higher content of titanium allows getting the greater content of a  $WB_4$  phase. Moreover, accurate comparison of spectra allows noticing small differences caused by the presence of titanium in the crystal lattice of  $WB_2$  or  $WB_4$  phases.

XRD diffractograms (Fig. 1) indicate low content of  $TiB_2$  phase and confirm that titanium dissolves well in the  $WB_4$  phase. With increasing titanium content the  $TiB_2$  phase increases (the positions of  $TiB_2$  are marked with a dashed line). Moreover,  $WB_4$  peaks are shifted to a lower  $2\theta$  angle. This effect can be explained by the increase in the interplanar distances due to the dissolution of titanium in the crystal lattice of the  $WB_4$  phase. In Fig. 2 an exemplary cross-section SEM-BSE images are shown. In the case of  $WB_{4.5}$  target two phases are seen. The dark, grey phase contains pure boron, whereas white areas are a mixture of  $WB_2$  and  $WB_4$  phases and were marked in Fig. 2a as  $WB_x$ . In Fig. 2b ( $W_{0.84}Ti_{0.16}B_{4.5}$  target) the effect of titanium addition on microstructure of obtained targets is observable. The addition of titanium results in a

decrease of dark boron areas and appearing of light grey islands of titanium diboride (Fig. 2b). The alloying also causes the fragmentation of white  $WB_x$  ( $WB_4 + WB_2$  mixture) grains.

More details about chemical composition and other properties of W-B and W-Ti-B targets were presented in [30,49].

### 3.2. W-Ti-B films

#### 3.2.1. Chemical composition and microstructure

The results of films chemical composition obtained by EDS method are presented in Table 2 and Fig. 3.

As it is seen in Table 2 the stoichiometry of used targets is not preserved. The difference in tungsten to titanium ratio in targets and in films respectively decreases with increasing of titanium addition. For example for sample W-B-Ti#8 Ti/(Ti + W) ratio in target is 0.08 when in coating 0.065 respectively. In the case of W-B-Ti#24 sample it is 0.24 and 0.196 respectively. At the same time, the content of boron increase from 64.2 at.% to 66.4 at.% for sample W-B-Ti#8 and W-B-Ti#24 respectively (Fig. 3c). A similar phenomenon was observed by Grančič et al. [50], where with the increasing of amount of heavy element (tantalum) the content of boron decreased. It can be seen also the amount of boron in relation to transition metals decreased from 4.5 in targets to 1.9 in W-B-Ti#0 and  $\sim 2.4$  in W-B-Ti#24 coating. It should be noted, when the boron content is measured with EDS method the result may be inaccurate. It is caused by the overlapping the peak of carbon and the peak of boron in the vicinity of 0.25 keV (Fig. 3b). The loss of titanium and boron was observed during previous works [17,37] and may be related to scattering caused by collisions with heavier elements in the plasma plume. The second reason of the decrease in the amount

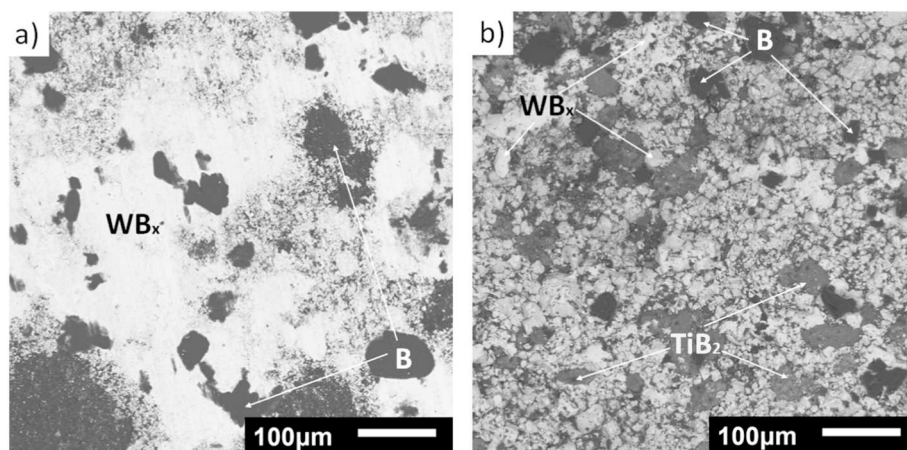


Fig. 2. Cross-section SEM-BSE images of SPS targets a)  $WB_{4.5}$ , b)  $W_{0.84}Ti_{0.16}B_{4.5}$ .

**Table 2**

Target composition, coating thickness, growth rate and chemical composition of the coatings measured by EDS.

Name	Target composition	Film thickness ( $\mu\text{m}$ )	Deposition rate (nm/min)	Concentration (at.%)			
				W	Ti	B	O
W-B-Ti#0	WB <sub>4.5</sub>	0.91	20.2	33.5	0	64.2	2.3
W-B-Ti#8	W <sub>0.92</sub> Ti <sub>0.08</sub> B <sub>4.5</sub>	0.92	20.4	28.5	2.0	64.8	4.8
W-B-Ti#16	W <sub>0.84</sub> Ti <sub>0.16</sub> B <sub>4.5</sub>	0.93	20.6	26.1	3.6	65.3	5.2
W-B-Ti#24	W <sub>0.76</sub> Ti <sub>0.24</sub> B <sub>4.5</sub>	0.93	20.7	22.6	5.5	66.4	5.6

of boron can be the resputtering of boron from the surface of the deposited layer. The  $> 2.1$  (titanium alloyed coatings) ratio of boron to transition metals means that (W,Ti)B<sub>2</sub> is supersaturated [19]. A further increase in the amount of boron could result in the formation of WB<sub>4</sub> phase, however, the energy balance on the surface of the sample prevents such solution. The transition to higher tungsten borides is observed during pulsed laser deposition WB<sub>x</sub> where the energies of the arriving particles are much higher compared to the sputtered by RF magnetron [51].

However, the rise of titanium content in the deposited layers can increase the amount of oxygen from 2.3 to 5.6 at.% for W-B-Ti#0 and W-B-Ti#24, respectively (Fig. 3c). This is probably due to the higher chemical activity of titanium compared to tungsten. For example the heat of formation  $-\Delta H_f^0$  of TiO is 518.7 kJ/mol [52] and is smaller than WO<sub>2</sub> (589.1 kJ/mol) [53].

The Fig. 4 presents XRD patterns of (W,Ti)B<sub>2</sub> films deposited from targets with different titanium content. It was observed that the films structure strongly depends on titanium addition. The films deposited from the target without titanium had AlB<sub>2</sub>-type WB<sub>2</sub> structure with (0001) preferred orientation (Fig. 4a). Low content of titanium  $C_{Ti} = 2.0$  at.% in sample W-B-Ti#8 (Fig. 4b) caused formation of wide and unclear spectrum indicating amorphous structure of the deposited film. Further increase of titanium content caused growth of AlB<sub>2</sub>-type

(W,Ti)B<sub>2</sub> films, and in W-B-Ti#24 coating, the single phase AlB<sub>2</sub>-type (W,Ti)B<sub>2</sub> was observed. The peak (0001) was broader and shifted to lower  $2\theta$  angles in comparison with that from films without titanium (Fig. 4a). Additionally reflections from other planes appeared. In the Fig. 5b the presence of amorphous structure has been confirmed by selected area electron diffraction (SAED). The image taken from film confirmed the occurrence of the amorphous layer (blurred diffraction rings) on the crystalline Si substrate (visible diffraction spots). In Fig. 5a W-B-Ti#0 coating with dense columnar-like microstructure was observed. The directional growth was typical for magnetron deposited films from WB<sub>2</sub> [22,36] or WB<sub>2.5</sub> [17] targets. Further increase in the amount of boron to 4.5 in relation to tungsten and titanium in targets did not change the morphology of deposited films. Similar structure was observed by Mayrhofer et al. [54] for overstoichiometric boron in TiB<sub>2</sub> films deposited by magnetron sputtering. Deposited films had also a columnar structure, with an average feature size of 20 nm, and (0001) preferred orientation. Columns were encapsulated in excess B and were themselves composed of smaller stoichiometric TiB<sub>2</sub> subcolumns with separated by a thin B-rich tissue phase of thickness 1–2 monolayers what caused their superhardness [54]. With the increasing content of titanium in deposited coatings, the columnar-like microstructure changed to the very dense and compact featureless morphology. TEM cross-section images of W-B-Ti#8 and W-B-Ti#16 films were similar to

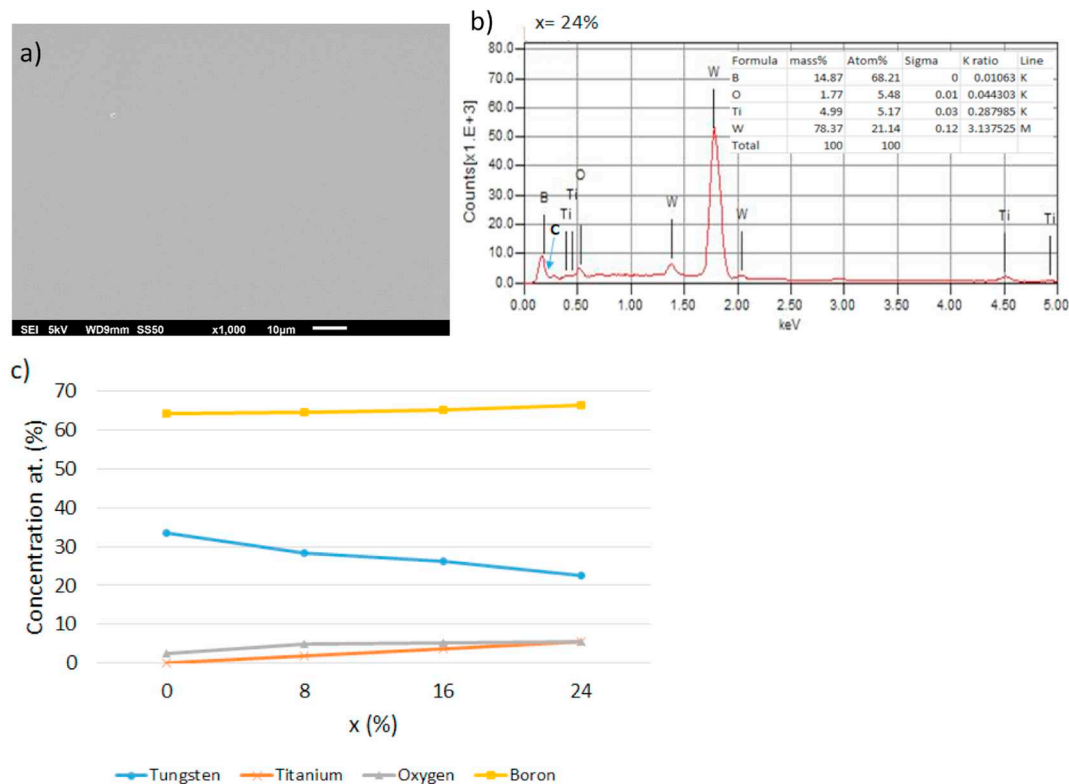


**Fig. 3.** Exemplary EDS analysis of the W-B-Ti#24 coating a) SEM image of the investigated area, b) EDS spectra and elemental composition of the film, c) the effect of titanium content in the target on the chemical composition of the deposited films.

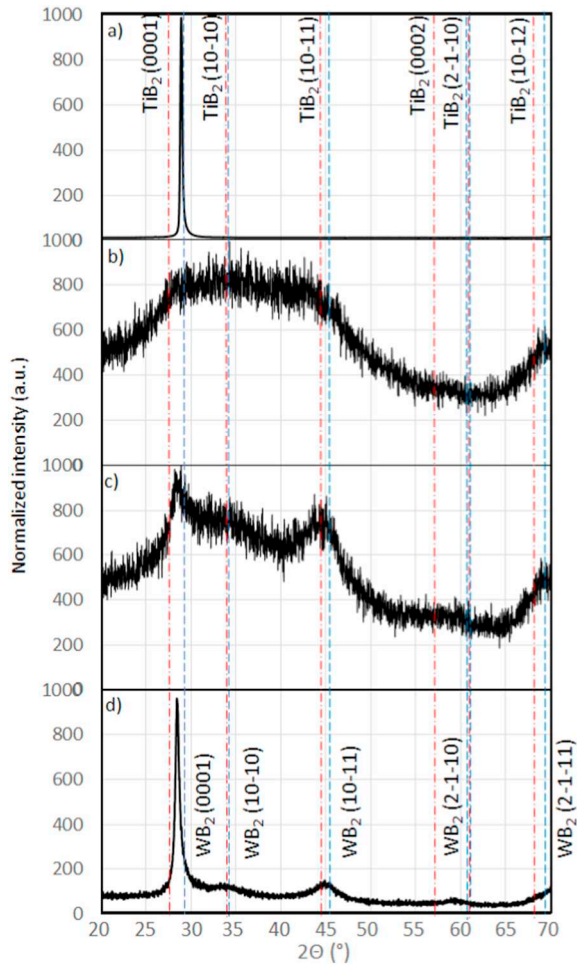


**Fig. 4.** X-ray diffraction patterns of deposited films a) W-B-Ti#0, b) W-B-Ti#8, c) W-B-Ti#16, d) W-B-Ti#24. Blue dashed line – theoretical positions of  $\alpha$ -WB<sub>2</sub> phase peaks ( $a = 3.010 \text{ \AA}$ ,  $c = 3.050 \text{ \AA}$  [1]) and red dashed-dot lines - theoretical positions of P<sub>6</sub>/mmm TiB<sub>2</sub> peaks ( $a = 3.035 \text{ \AA}$ ,  $c = 3.223 \text{ \AA}$  [55]). (For interpretation of the references to colour in this figure legend, the reader is referred to the web version of this article.)

W-B-Ti#24 film (Fig. 5b), and all of them presented the featureless morphology.

Similar morphology was observed by Sobol et al. [19] due to DC magnetron sputtering of targets made of WB<sub>2</sub> and TiB<sub>2</sub> powders. The deposited films with a small content of titanium atoms possessed an unoriented structure. At a content of Ti  $\approx 10.2 \text{ at.}$ %, a columnar growth of crystallites was observed [19]. The change of morphology after the titanium addition could be explained on the basis of Thornton's structural zone model (SZM) of sputtered films extended to the region of low sputtering gas pressures [56]. The used deposition conditions i.e. argon pressure  $p_{Ar} = 0.9 \text{ Pa}$ , substrate temperature  $T_s = 520 \text{ }^\circ\text{C}$  and melting temperature of WB<sub>2</sub> =  $2365 \text{ }^\circ\text{C}$  indicated that films deposited without titanium were in the region of "ZONE 1" where columnar crystallites separated by voids were formed. In this region the films were under tensile macrostress  $\sigma > 0$ . The addition of titanium caused the increase of  $T_s/T_m$  ratio due to lowering of melting temperature of (W,Ti)B<sub>2</sub> and change of macrostress to the compressive [57]. As a result the dense voids-free microstructure was formed (ZONE T) [56,58].

Figs. 6 and 7 present high resolution TEM images of W-B-Ti#8 and W-B-Ti#24 samples studied in a plane-view. The sample W-B-Ti#24 (Fig. 6a) was cut evenly. In the case of W-B-Ti#8 (Fig. 7a), the sample is a little crooked, which was caused by the relatively small thickness of the film. The main aim of the TEM study was to investigate the structure of the mentioned two different states. As was expected, both layer structures indicate an amorphous character. It cannot be observed any grains or columnar structures (Figs. 6b and 7b). Furthermore, the additional fast Fourier transform (FTT) has been carried out (Figs. 6c and 7c) to show whether the material is amorphous or crystalline. As it can be seen on obtained FTT images, the presence of the amorphous layer (blurred diffraction rings) has been confirmed in two obtained films. The results of the FTT investigation are consistent with SAED study (insert of Fig. 5b), in which the amorphous halo confirms the presence of the amorphous phase.

Worth noting is the absence of peaks corresponding to Ti and TiB<sub>2</sub> phase on the X-ray diffraction pattern of the deposited films (Fig. 4). In order to estimate the chemical state of deposited coatings, the XPS analysis was performed (see Fig. 8). Conducted research indicates that Ti-doped films were similar to each other in relation to chemical state. However, they were different taking into account the quantitative chemical composition. The binding energy for deposited films varied

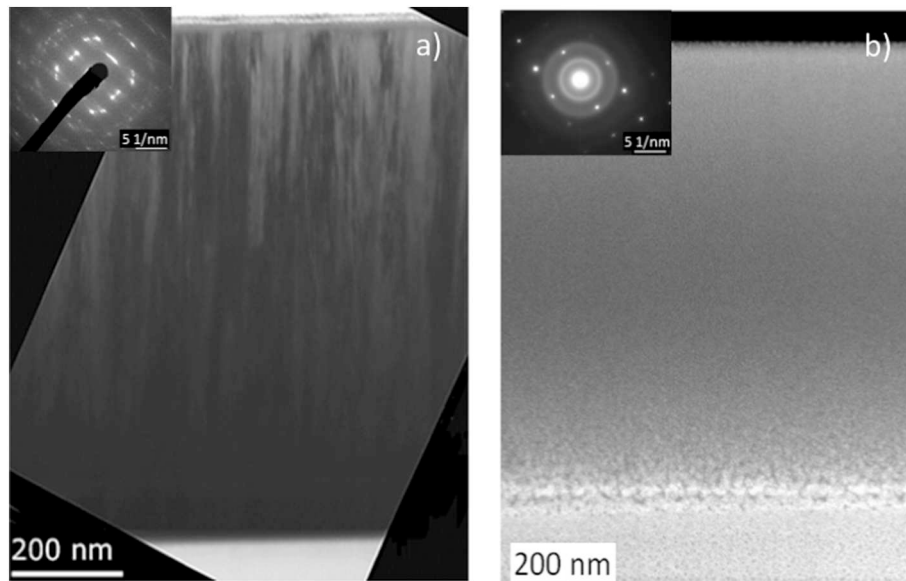


**Fig. 5.** Cross-section Bright-Field TEM images of deposited films (a) W-B-Ti#0 and (b) W-B-Ti#24. Inserts present corresponding SAED patterns.

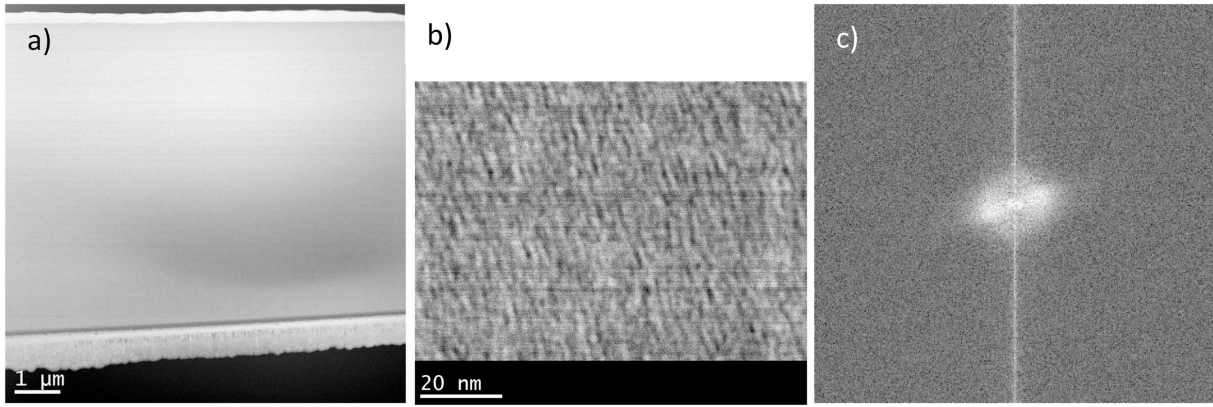


Fig. 6. Plane-view high-resolution TEM images of W-B-Ti#24 coating performed in: a) 10 k magnification, b) 1000 k magnification and c) 1000 k magnification with the fast Fourier transform (FTT) analysis.

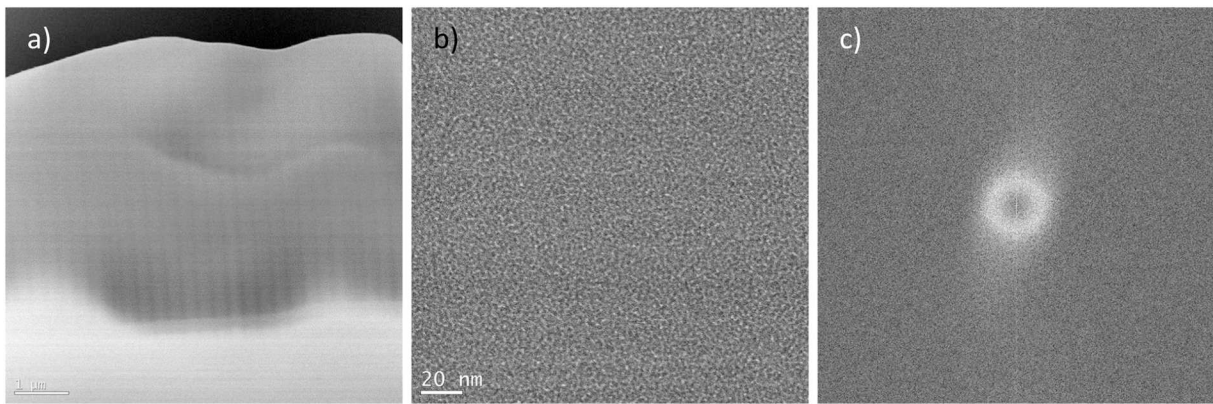


Fig. 7. Plane-view high-resolution TEM images of W-B-Ti#8 coating performed in: a) 15 k magnification, b) 1000 k magnification and c) 1000 k magnification with the fast Fourier transform (FTT) analysis.

from 30.7 to 31.2 eV for the  $W4f_{7/2}$  peak and from 187.9 to 188.4 eV for  $B1s$  (187.8 eV for pure boron [59]), which is consistent with the literature data and corresponds to  $W_2B_5$  phase [60]. The comparison of presented values with the  $W4f_{7/2}$  peak of pure W centred at 31.4 eV [61] showed shift to the lower-energy side. The shift to lower energy can be explained by the electronegativity of boron (EN = 2.04) which

was lower than that of tungsten (EN = 2.36). When oxygen with electronegativity (EN = 3.44) for example is investigated, the shift to higher energy is observed and the change gets greater due to increasing oxidation. When titanium is added the  $Ti2p_{3/2}$  peak with binding energy from 454.6 to 454.8 eV appears. The shift from position 454.0 for pure titanium [62] indicates the formation of  $TiB_2$  phase. As it was

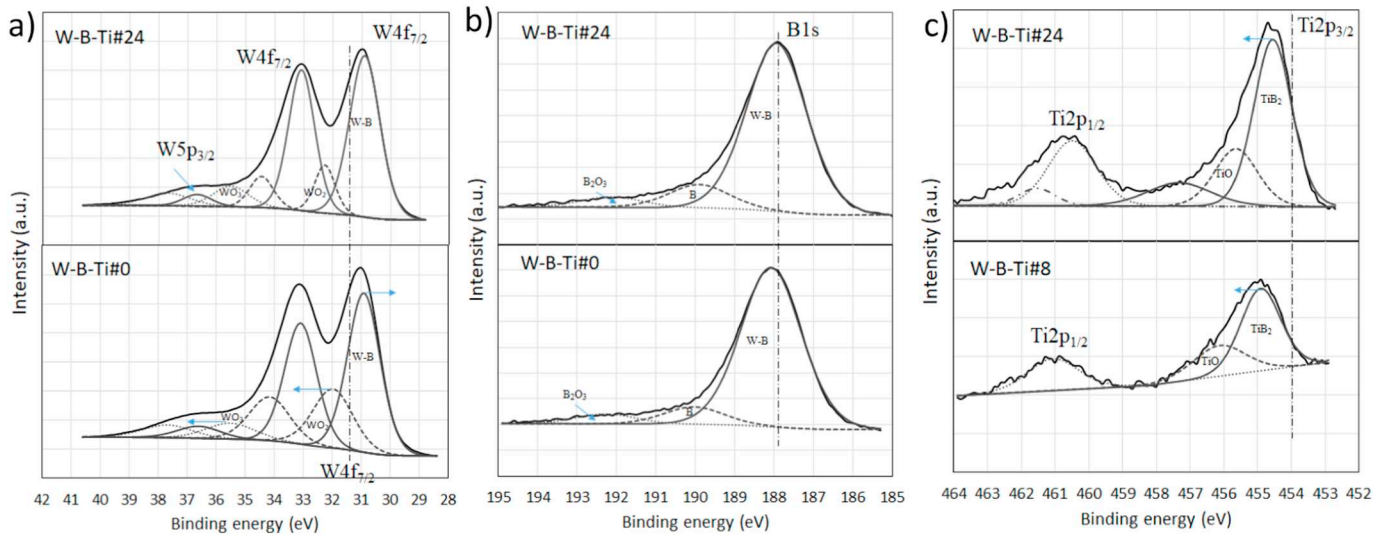


Fig. 8. XPS spectra of W-B-Ti#0 and W-B-Ti#24 coatings. a) high-resolution spectrum of binding energy corresponding to  $W4f_{7/2}$ ,  $W4f_{5/2}$  and  $W5p_{3/2}$  electron states, b)  $B1s$  c)  $Ti2p_{1/2}$  and  $Ti2p_{3/2}$ . The vertical dashed line indicates the binding energy of pure elements. The horizontal arrows show the direction of shift due to change of chemical status.

shown in [10,48] tungsten borides poses great possibility to alloying by other metals. Titanium occupies the positions of voids in the crystal lattice and change the properties of alloyed tungsten borides [19,36]. The surplus of the doping element may react with boron and form compounds with a structure similar to  $WB_2$ . The addition of titanium cause the formation of  $TiB_2$  which has similar hexagonal structure ( $P6_{/mmm}$ ) as  $\alpha-WB_2$  [3].

The appearance of a new phase in the structure of the deposited layers does not change the X-ray diffraction pattern, however the positions of the  $WB_2$  peaks are shifted towards the corresponding positions of the  $TiB_2$  peaks, i.e. towards smaller angles (Fig. 4). The Fig. 8c shows that  $TiB_2$  phase is present in all coatings deposited from Ti alloyed targets. In deposited films the XPS spectra show also presence of tungsten oxides ( $WO_2$ ,  $WO_3$ ), titanium oxide ( $TiO$ ,  $Ti_2O_3$ ) and contamination with carbon, carbon in carbides, carbon in oxidized state and nitrogen. Carbide was not indicated on the high resolution XPS tungsten spectra because the signal from W–C bonds coincides with the range for W–O bonds correspond to  $WO_2$  species. It should be remembered that the XPS method is a surface method and the signal is collected from a layer of three average free paths of electron. Even after 5 min Ar ion beam etching and removal of 7 nm of surface layer the content of oxygen is still high.

### 3.2.2. Mechanical and tribological properties

On the basis of previous publications taking into account tungsten borides coatings [18,19,21] the optimal indentation load for measurement of mechanical properties should lay in the flat region of hardness–displacement curve up to formation of first crack in coating. For this load the deformation in the contact is in full plasticity regime. Additionally, to minimize the effect of the substrate, the hardness and elastic modulus values should be calculated based on the average data obtained at depths  $< 1/10$  of the layer thickness [63]. Accordingly to those assumptions, a load of 7 mN was chosen to determine the mechanical properties. In the Fig. 9 the mechanical properties of films deposited from targets with different titanium content are presented. The mechanical properties of coatings are characterized by the hardness  $H$  and the effective elastic modulus

$$\frac{1}{E^*} = \frac{1 - \nu^2}{E} + \frac{1 - \nu_i^2}{E_i} \quad (1)$$

where  $E$  is the elastic modulus, and  $\nu$  is the Poisson's ratio ( $\nu = 0.3$  [64]), subscript  $i$  means indenter. Also the elastic recovery  $W_e$  and the ratio  $H/E^*$ , which can determine the films crack resistance to a certain extent, are used to evaluate the mechanical behaviour of the films.

The deposited films without titanium had similar properties as presented in [17,18,23]. Due to the crystalline columnar structure hardness reached  $49.0 \pm 0.6$  GPa with effective elastic modulus of  $709.4 \pm 89.5$  GPa. The elastic recovery  $W_e$  and the ratio  $H/E^*$  were below 0.6 and 0.1, respectively, what means that they were not flexible and not resistant to cracking [56,58]. As it is shown in the Fig. 9 the addition of 2 at.% of Ti (coating W-B-Ti#8) caused a two-fold decrease of the hardness and elastic modulus. Due to parameters presented by

Musil [56] the nature of the layers also changed. The elastic recovery was still under 0.6 but ratio  $H/E^*$  was  $> 0.1$ . It was a result of changing highly oriented crystalline structure to amorphous and the appearance of the  $TiB_2$  phase. According to the reports on the similar systems [26,65], the absence of dislocation activity in the small nanocrystals and the formation of a strong interface between the two phases could greatly reduce the crack formation and propagation. The increasing of titanium content to  $C_{Ti} \approx 3.6$  at.% (W-B-Ti#16 coating) caused about 20% rise of the hardness and effective elastic modulus to  $37.5 \pm 1.9$  GPa and  $341.2 \pm 2.4$  GPa, respectively. At the same time the  $W_e$  and the ratio  $H/E^*$  reached value 0.685 and 0.11, respectively. The highest hardness  $H = 39.2 \pm 1.5$  GPa was measured for  $C_{Ti} \approx 5.5$  at.% (W-B-Ti#24 coating). The increasing of titanium content from 3.6 to 5.5 at.% slightly increased value of other parameters. The deposited films were very hard, flexible and resistant to cracking at the same time. The phase of  $\alpha-WB_2$  (Fig. 4d) was stabilized by hexagonal nanocrystals of  $TiB_2$ , which may block dislocation movement. The better elastic properties were also the results of change of structure from columnar to voids-free solid nanocrystalline material (ZONE T). When the grain size is smaller than the length of dislocation, the dislocations are not generated and processes in grain boundary regions play a dominant role. In the case of a nanocomposite which consists coherently coupled grains of two phases (with good correspondence between the periods of crystal lattices at the phase boundary) the binding strength is increased [19,66]. According to Fig. 4, such a structure was made on the basis of the coincidence of the interplanar distances of two phases  $\alpha-WB_2$  ( $a = 3.010 \text{ \AA}$ ,  $c = 3.050 \text{ \AA}$ ) and  $P6_{/mmm} TiB_2$  ( $a = 3.035 \text{ \AA}$ ,  $c = 3.223 \text{ \AA}$ ). The creation of consistent boundaries between nanocrystals of different phases increased the strength of the composite. Formation of coherent boundaries between grains caused suppression of grain-boundary sliding in monocrystalline materials [19]. This led to increased mechanical properties of deposited films.

The Fig. 10 shows the average values of the wear track width and depth after wear process as a measure (characteristic) of W-B-Ti-layer wear. The tribological test was conducted for of the coating W-B-Ti#24. Values of the depth and width of the groove were  $0.26 \mu\text{m}$  and  $30 \mu\text{m}$  at a load of 0.3 N, and  $0.41 \mu\text{m}$  and  $43 \mu\text{m}$  at a load of 0.5 N, respectively. As it was shown earlier WB coating were many times more resistant to wear than steel [18]. In Fig. 10b a comparison of present investigation to those results are shown. As it is presented in Fig. 10a, with the same diameter of the counterspecimen  $Al_2O_3$  ball (6 mm) and under a similar normal load force than in [18], the coating with titanium addition had a higher wear resistance. This behaviour of coating resulted from the structure of the compared layers. The titanium-alloyed layer, due to its compact structure, had a lower hardness, however the crack resistance was higher. The non-columnar structure contained fewer defects, which made it more ductile and resistant to cracking.

Further studies showed, that the friction coefficient was lower for the W-B-Ti#24 layer than for the WB layer (Fig. 11). For the W-B-Ti#24 coating, the friction coefficient was stable with very low value in the range  $0.12 \div 0.15$  during 1 h of wear test. In the case of unalloyed layer W-B-Ti#0 the friction coefficient oscillated close to 0.2 but at first part

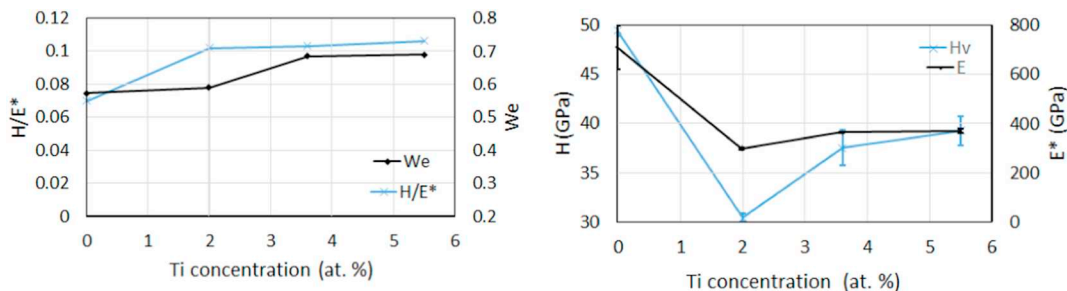
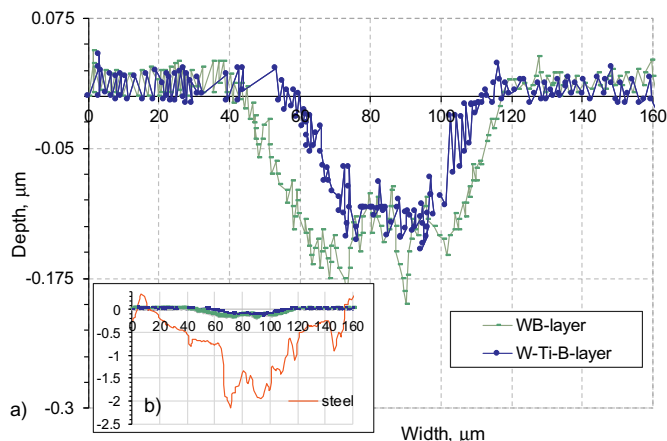
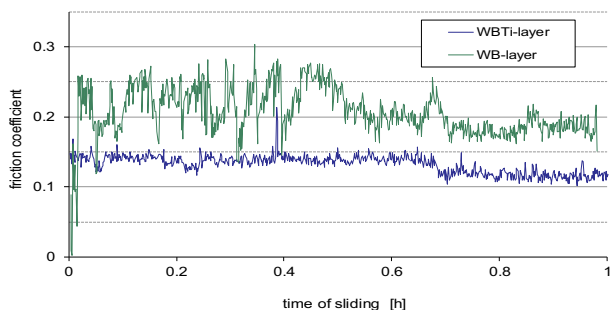


Fig. 9. Mechanical properties of the deposited films in function of Ti concentration. On the left results of hardness  $H$  and effective elastic modulus on the right results of elastic recovery  $W_e$  and  $H/E^*$ .



**Fig. 10.** The depth and width a) of wear track on W-B-Ti#24 layer under normal loads of 0.3 N at sliding time of 1 h with comparison to wear characteristics of WB-layer from [18] a) and inset - comparison to wear characteristics of 304 stainless steel substrate b).



**Fig. 11.** The time-dependent behaviour of the friction coefficient of W-B-Ti#24 and W-B-Ti#0 coatings.

of test there were great dispersions from 0.19 to 0.28. After 30 min the average friction stabilizes.

This behaviour was related the removal of contaminants from the wear track (Fig. 12a). Because the addition of titanium increased crack resistance, less defects and contaminants appeared and the shape of the groove was regular throughout the measurement (Fig. 12b).

### 3.2.3. Corrosion resistance

Electrochemical spectroscopy impedance results are presented for coatings alloyed with Ti on Nyquist and Bode plots (Fig. 13). They are illustrating the same measuring setup and are mutually exclusive. Nyquist plot represents the relation between real and imaginary impedance while Bode plot shows correlation between phase shift angle and module of impedance magnitude depending on measuring frequency.

On Nyquist plot (Fig. 13a) parts of semicircles was recognized, which represents the coating-solution contact. Wider diameter means

greater electrical resistance and as a result better corrosion resistance. In this case coating with W-B-Ti#8 prove better electrochemical resistance then samples with higher Ti content. Creation of second smaller semicircles for W-B-Ti#16 and W-B-Ti#24 represents the diffusion in active surface and electrolyte (mass transport). Bode plot (Fig. 13b) confirm presented accuracy by comparing different factors. Phase curve (thin lines) and impedance magnitude (thick lines) shows that again W-B-Ti#8 coating has better corrosion resistance properties, while the other two samples are at similar level.

Potentiodynamic polarization results for the (W,Ti)B<sub>2</sub> coated stainless steel 304 substrate and the original substrate in a 0.5 M NaCl solution are shown in Fig. 12 and Table 3. Additionally, the protective efficiency,  $P_i$  (%), which is opposite of porosity of the films, was calculated from Eq. 2 [67].

$$P_i (\%) = \left( 1 - \frac{I_{corr}}{I_{corr}^0} \right) \times 100 \quad (2)$$

where  $I_{corr}$  and  $I_{corr}^0$  represent the corrosion current density in the presence and absence of a coating, respectively.

There was a considerable decrease in the anodic current of the samples with deposited films compared to the uncoated 304 SS. It is well known that the  $I_{corr}$  is important parameter to evaluate kinetics of corrosion reaction. Corrosion protection is normally proportional to the  $I_{corr}$  measured via polarization [68]. The deposition of WB<sub>2</sub> films caused lowering of the current density in relation to 304 SS from 2.008 to 0.673  $\mu\text{A cm}^{-2}$  what was in good agreement with result presented in ref. [26]. However, the addition of titanium caused further improvement of the corrosion resistance. The current density for the sample coated with (W,Ti)B<sub>2</sub> film with  $C_{Ti} = 5.5$  at.% (W-B-Ti#24) was about one order of magnitude lower than that of the uncoated 304 SS (Fig. 14 and Table 3). As it was shown in the Fig. 5 the addition of titanium to the WB<sub>2</sub> caused that films were more dense and lost their columnar structure. As a result less direct diffusion path for the corrosive medium were formed what resulted in the improvement of corrosion resistance. In the case of the pure WB<sub>2</sub> films, the columnar structure provided the straight diffusion channels for corrosive medium, which may accelerate the corrosion behaviour.

The best protective efficiency  $P_i = 96.1\%$  was achieved for W-B-Ti#8 coating. The corrosion protection efficiency of this coating was evident from both the increase in corrosion potential and the reduction in the corrosion current density. Because hydrogen evolution takes place during potentiodynamic test at iron surface in pores, hence the coating substrate adhesion plays important role. The adhesion of film W-B-Ti#8 to substrate was probably greater than that of coatings with higher titanium content due to more gradual transition of hardness and elastic modulus across coating substrate interface. Therefore, the protective efficiency drops with the rise of titanium content and the associated increase in hardness.

## 4. Summary

In this work the effects of titanium content on the properties of thin films deposited by RF magnetron sputtering from spark plasma sintered

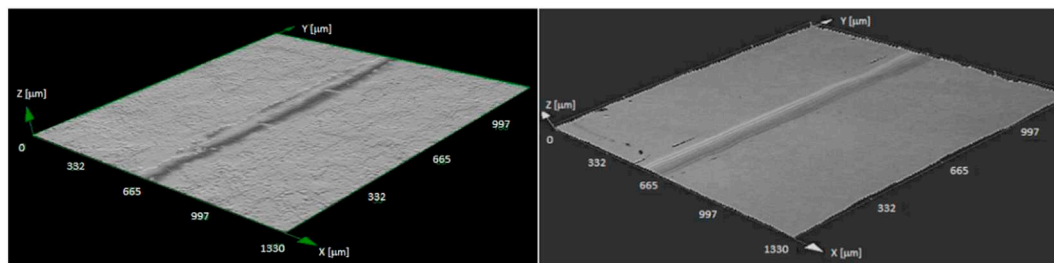


**Fig. 12.** Profiles of wear track measured by scanning profilometry technique: a) W-B-Ti#0 coating and b) W-B-Ti#24 coating.

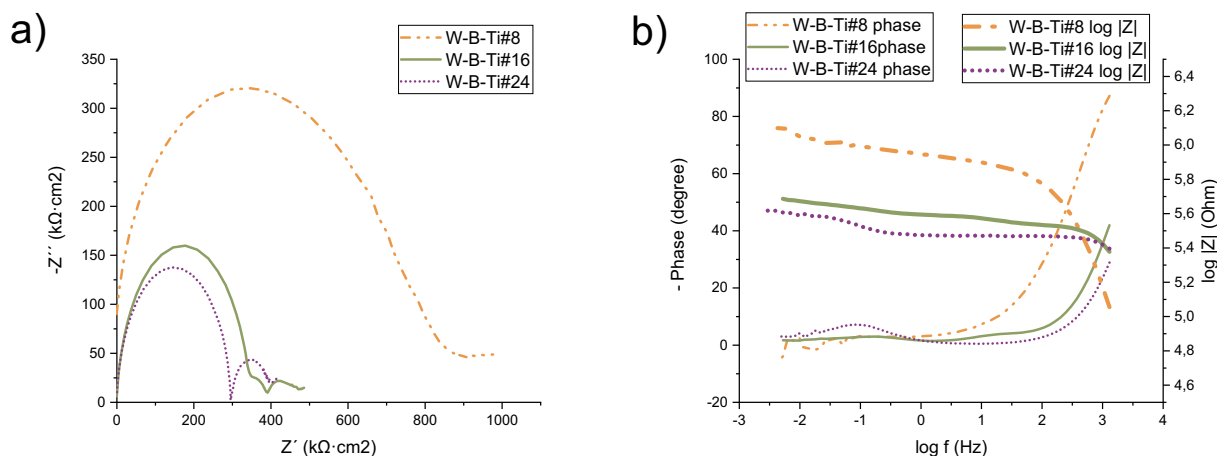


Fig. 13. Electrochemical spectroscopy impedance results for coatings alloyed by titanium. a) Nyquist and b) Bode plot.

Table 3

Values of corrosion potential ( $E_{corr}$ ) corrosion current density ( $I_{corr}$ ) and protective efficiency ( $P_i$ ) for 304 stainless steel substrate and deposited films in 0.5 M NaCl solution.

Material	$E_{corr}$ (mV)	$I_{corr}$ ( $\mu\text{A cm}^{-2}$ )	Protective efficiency $P_i$ (%)
Stainless steel 304	-325.8	2.008	-
$C_{Ti} = 0$ (W-B-Ti#0)	-478.6	0.673	66.5
$C_{Ti} = 2.0$ at.% (W-B-Ti#8)	-156.0	0.078	96.1
$C_{Ti} = 3.6$ at.% (W-B-Ti#16)	-543.2	0.187	90.7
$C_{Ti} = 5.5$ at.% (W-B-Ti#24)	-485.4	0.210	89.5

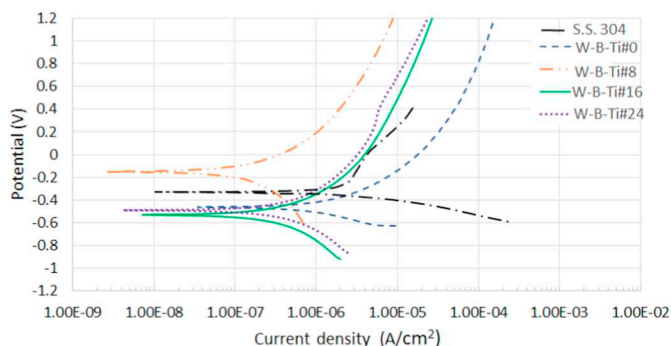


Fig. 14. Polarization curves of stainless steel substrate and coatings with different Ti concentration content in 0.5 M NaCl solution.

(SPS) targets are presented. The effect of adding titanium was evident in both sintered targets and deposited layers. Even if almost stoichiometric atomic content of boron (4.5) was used, the addition of 8 at.% Ti caused formation of 94.5%  $WB_4$  phase, when without titanium it was only 8.2%  $WB_4$ . In spite of using of  $W_{1-x}Ti_xB_{4.5}$  targets, the films deposited by RF MS method were mainly composed with  $AlB_2$ -type  $WB_2$  phase. The overstoichiometric boron was lost due to scattering on heavy particles in the plasma plume and resputtering from the films surface. The  $WB_2$  coatings deposited without titanium had crystalline columnar structure with 0001 preferred orientation. The superhardness of deposited films  $H = 49 \pm 0.6$  GPa could be explained by inhibition of nucleation and gliding of dislocations due to small dimension across the  $WB_2$  nanocolumns and also the high cohesive strength of the thin B-rich tissue phase which prevents grain-boundary sliding. In opposite to well-known columnar  $\alpha$ - $WB_2$  magnetron sputtered coatings, the addition of titanium to deposited films caused that they were formed in the

zone T of the Thornton's Structural Zone Model and created flexible hard nanocomposite coatings. The investigations showed that the alloying by titanium apparently leads to the change of the structure from columnar to dense, compact structure with featureless morphology. The introducing of titanium caused change of crystalline to amorphous phase and next with higher content of titanium the hexagonal  $\alpha$ -(W,Ti)  $B_2$  structure is formed. Such change is due to lowering of melting temperature of synthesized material and increasing of the particle energy arriving to the film surface by the using RF against DC generator. Obtained films are simultaneously hard  $H > 37.5$  GPa, exhibit high values of the hardness and effective Young's modulus  $E^*$  ratio  $H/E^* > 0.1$ , elastic recovery  $W_e > 60\%$ , compressive macrostress  $\sigma < 0$  and dense, void-free microstructures. It can be stated that the (W,Ti) $B_2$  coatings have better tribological properties than superhard WB layers. During 1 h of wear test the friction coefficient of alloyed coatings was stable with very low value in the range  $0.12 \div 0.15$ . Moreover, titanium addition improved anticorrosive properties. The change from columnar to dense and crystalline/amorphous structure caused less direct diffusion path for the corrosive medium. As a result the protective efficiency reached 96% in comparison with uncoated surface of 304 SS.

#### CRedit authorship contribution statement

**Tomasz Moscicki:** Conceptualization, Writing - original draft, Writing - review & editing. **Rafal Psiuk:** Investigation, Formal analysis. **Hanna Stomińska:** Investigation. **Neonila Levitant-Zayonts:** Investigation. **Dariusz Garbiec:** Investigation. **Marcin Pisarek:** Investigation. **Piotr Bazarnik:** Investigation. **Szymon Nosewicz:** Writing - review & editing. **Justyna Chrzanowska-Gizyńska:** Writing - review & editing, Investigation.

#### Declaration of competing interest

The authors declare that they have no known competing financial interests or personal relationships that could have appeared to influence the work reported in this paper.

#### Acknowledgement

This work was supported by the National Science Centre, Poland [grant number 2017/25/B/ST8/01789].

#### References

- [1] C. Fuger, V. Moraes, R. Hahn, H. Bolvardi, P. Polcik, H. Riedl, P.H. Mayrhofer, Influence of tantalum on phase stability and mechanical properties of  $WB_2$ , MRS

- Communications 9 (1) (2019) 375–380.
- [2] V. Moraes, H. Riedl, C. Fuger, P. Polcik, H. Bolvardi, D. Holec, P. Mayrhofer, Ab initio inspired design of ternary boride thin films, *Sci. Rep.* 8 (2018) 9288.
- [3] G. Akopov, M. Yeung, M. Kaner, Rediscovering the crystal chemistry of borides, *Adv. Mater.* 29 (2017) 1604506.
- [4] G. Akopov, N. Pangilinan, R. Mohammadi, R. Kaner, Perspective: Superhard metal borides: a look forward, *APL Materials* 6 (2018) 70901.
- [5] P.J. Robinson, G. Liu, S. Ciborowski, C. Martinez-Martinez, J.R. Chamorro, X. Zhang, T.M. McQueen, K.H. Bowen, A.A. Alexandrova, Mystery of three borides: differential metal–boron bonding governing superhard structures, *Chem. Mater.* 29 (2017) 9892–9896.
- [6] Y. Liang, Z. Wu, X. Yuan, W. Zhang, P. Zhang, Discovery of elusive structures of multifunctional transition-metal borides, *Nanoscale* 8 (2016) 1055–1065.
- [7] M. Maździarz, T. Mościcki, Structural, mechanical and optical properties of potentially superhard WBx polymorphs from first principles calculations, *Mater. Chem. Phys.* 179 (2016) 92–102.
- [8] Y. Liang, P. Qin, H. Jiang, L. Zhang, J. Zhang, C. Tang, Designing superhard metals: the case of low borides, *AIP Adv.* 8 (2018) 045305.
- [9] X.Y. Cheng, X.Q. Chen, D.Z. Li, Y.Y. Li, Computational materials discovery: the case of the W-B system, *Acta Cryst C70* (2014) 85–103.
- [10] G. Akopov, I. Roh, Z.C. Sobell, M.T. Yeung, L. Pangilinan, C.L. Turner, R.B. Kaner, Effects of variable boron concentration on the properties of superhard tungsten tetraboride, *J. Am. Chem. Soc.* 139 (2017) 17120–17127.
- [11] L.E. Pangilinan, C.L. Turner, G. Akopov, M. Anderson, R. Mohammadi, R.B. Kaner, Superhard tungsten diboride-based solid solutions, *Inorg. Chem.* 57 (2018) 15305–15313.
- [12] F. Zhao, L. Qiu, Z. Ding, Y. Li, B. Yao, W. Shen, L. Quan, P. Zhu, Synthesis and characterization of WB2-WB3-B4C hard composites, *Int. J. Refract. Met. Hard Mater.* 82 (2019) 268–272.
- [13] A.H. Shaw, *Physical Properties of Various Conductive Diborides and Their Binaries, Graduate Theses and Dissertations* (2015), p. 14496 <https://lib.dr.iastate.edu/etd/14496>.
- [14] L. Yang, K. Zhang, M. Wen, Z. Hou, C. Gong, C. Hu, X. Cui, W. Zheng, Highly hard yet toughened bcc-W coating by doping unexpectedly low B content, *Sci. Rep.* 7 (2017) 9353.
- [15] L. Yang, K. Zhang, Y. Zeng, X. Wang, S. Du, C. Tao, P. Ren, X. Cui, M. Wen, Boron doped bcc-W films: achieving excellent mechanical properties and tribological performance by regulating substrate bias voltage, *Appl. Surf. Sci.* 423 (2017) 275–282.
- [16] J. Willer, S. Pompil, D. Ristow, Sputter-deposited WBx films, *Thin Solid Films* 188 (1990) 157–163.
- [17] J. Chrzanowska, Ł. Kurpaska, M. Giżyński, J. Hoffman, Z. Szymański, T. Mościcki, Fabrication and characterization of superhard tungsten boride layers, *Ceram. Int.* 42 (2016) 12221–12230.
- [18] J. Chrzanowska-Giżyńska, P. Denis, S. Woźniacka, Ł. Kurpaska, Mechanical properties and thermal stability of tungsten boride films deposited by radio frequency magnetron sputtering, *Ceram. Int.* 44 (2018) 19603–19611.
- [19] O. Sobol, S. Dub, A. Pogrebnjak, R. Mygushchenko, A. Postelnyk, A. Zvyagolsky, G. Tolmachova, The effect of low titanium content on the phase composition, structure, and mechanical properties of magnetron sputtered WB2-TiB2 films, *Thin Solid Films* 662 (2018) 137–144.
- [20] O. Sobol, Influence of deposition conditions and annealing temperature on phase composition and structure of W-B system ion-plasma condensates, *Functional Materials* 13 (2006) 387–392.
- [21] C. Jiang, Z. Pei, Y. Liu, J. Xiao, J. Gong, C. Sun, Preparation and characterization of superhard AlB2-type WB2 nanocomposite coatings, *Phys. Status Solidi A* 210 (2013) 1221–1227.
- [22] Y. Liu, C. Jiang, Z. Pei, H. Lei, J. Gong, C. Sun, Microstructure and properties of AlB2-type WB2 thin films deposited by direct-current magnetron sputtering, *Surf. Coat. Technol.* 245 (2014) 108–116.
- [23] Y. Liu, R. Han, F. Liu, Z. Pei, C. Sun, Sputtering gas pressure and target power dependence on the microstructure and properties of DC-magnetron sputtered AlB2-type WB2 films, *J. Alloys Compd.* 703 (2017) 188–197.
- [24] Y. Liu, T. Li, F. Liu, Z. Pei, Thermal stability of WB2 and W–B–N films deposited by magnetron sputtering, *Acta Metallurgica Sinica (English Letters)* 32 (2019) 136–144.
- [25] H. Woods, F. Wawner, B. Fox, Tungsten diboride: preparation and structure, *Science* 151 (1966) 75.
- [26] Y. Liu, D. Deng, H. Lei, Z. Pei, C. Jiang, C. Sun, J. Gong, Effect of nitrogen content on microstructures and mechanical properties of WB2(N) films deposited by reactive magnetron sputtering, *J. Mater. Sci. Technol.* 31 (2015) 1217–1225.
- [27] V. Moraes, C. Fuger, V. Paneta, D. Primetzhofer, P. Polcik, H. Bolvardi, M. Arndt, H. Riedl, P.H. Mayrhofer, Stoichiometry and tantalum dependent thermal stability of  $\alpha$ -structured W-Ta-B thin films, *Scr. Mater.* 155 (2018) 5–10.
- [28] J.V. Rau, A. Latini, R. Teghil, A. De Bonis, M. Fosca, R. Caminiti, V.R. Albertini, Superhard tungsten tetraboride films prepared by pulsed laser deposition method, *ACS Appl. Mater. Interfaces* 3 (9) (2011) 3738–3743.
- [29] J. Chrzanowska-Giżyńska, P. Denis, J. Hoffman, M. Giżyński, T. Mościcki, D. Garbiec, Z. Szymański, Tungsten borides layers deposited by a nanosecond laser pulse, *Surf. Coat. Technol.* 335 (2018) 181–187.
- [30] T. Moscicki, J. Radziejewska, J. Hoffman, J. Chrzanowska, N. Levintant-Zayonts, D. Garbiec, Z. Szymański, WB2 to WB3 phase change during reactive spark plasma sintering and pulsed laser ablation/deposition processes, *Ceram. Int.* 41 (2015) 8273–8281.
- [31] N. Ohmae, A. Nakamura, S. Koike, M. Umeno, Formation of tungsten borides studied by field ion microscopy, *J. Vac. Sci. Technol. A* 5 (1987) 1367.
- [32] B.L. Ivanov, M.S. Wellons, C.M. Lukehart, Confined-plume chemical deposition: rapid synthesis of crystalline coatings of known hard or superhard materials on inorganic or organic supports by resonant IR decomposition of molecular precursors, *J. Am. Chem. Soc.* 131 (2009) 11744–11750.
- [33] O. Shovkoplyas, O. Sobol, Influence of thermal and radiation effects on the phase composition, structure and stress-strain state of Ti-W-B system coatings deposited from ion-atomic fluxes, *Journal OF Nano- And Electronic Physics* 6 (2014) 2024.
- [34] O. Sobol, Nanostructural ordering in W–Ti–B condensates, *Phys. Solid State* 49 (2007) 1161–1167.
- [35] O. Sobol, O. Grigoryev, Y. Kunitsky, S. Dub, A. Podtelezchnikov, A. Stetsenko, Peculiarities of structure state and mechanical characteristics in ion-plasma condensates of quasibinary system borides W2B5-TiB2, *Sci. Sinter.* 38 (2006) 63–72.
- [36] H. Euchner, P. Mayrhofer, H. Riedl, F. Klimashin, A. Limbeck, P. Polcik, S. Kolozsvari, Solid solution hardening of vacancy stabilized TixW1-xB2, *Acta Mater.* 101 (2015) 55–61.
- [37] J. Chrzanowska-Giżyńska, P. Denis, M. Giżyński, Ł. Kurpaska, I. Mihailescu, C. Ristoscu, Z. Szymański, T. Mościcki, Thin WBx and WyTi1–yBx films deposited by combined magnetron sputtering and pulsed laser deposition technique, *Appl. Surf. Sci.* 478 (2019) 505–513.
- [38] J. Berlin, Analysis of boron with energy dispersive x-ray spectrometry, *Imaging Microscopy* 13 (2011) 19–21.
- [39] G. Greczynski, L. Hultman, C1s peak of adventitious carbon aligns to the vacuum level: dire consequences for material’s bonding assignment by photoelectron spectroscopy, *ChemPhysChem* 18 (2017) 1507–1512.
- [40] G. Greczynski, L. Hultman, Reliable determination of chemical state in x-ray photoelectron spectroscopy based on sample-work-function referencing to adventitious carbon: resolving the myth of apparent constant binding energy of the C 1s peak, *Appl. Surf. Sci.* 451 (2018) 99–103.
- [41] W. Oliver, G. Pharr, An improved technique for determining hardness and elastic modulus using load and displacement sensing indentation experiments, *J. Mater. Res.* 7 (1992) 1564–1583.
- [42] T. Miura, Y. Benino, R. Sato, T. Komatsu, Universal hardness and elastic recovery in Vickers nanoindentation of copper phosphate and silicate glasses, *J. Eur. Ceram. Soc.* 23 (2003) 409–416.
- [43] N. Levintant-Zayonts, S. Starzynski, M. Kopec, S. Kucharski, Characterization of NiTi SMA in its unusual behaviour in wear test, *Tribol. Int.* 137 (2019) 313–323.
- [44] E. McCafferty, Validation of corrosion rates measured by the Tafel extrapolation method, *Corros. Sci.* 47 (2005) 3202–3215.
- [45] Y. Liang, Z. Fu, X. Yuan, S. Wang, Z. Zhong, W. Zhang, An unexpected softening from WB3 to WB4, *EPL (Europhysics Letters)* 98 (2012) 66004.
- [46] Q. Tao, D. Zheng, X. Zhao, Y. Chen, Q. Li, Q. Li, C. Wang, T. Cui, Y. Ma, X. Wang, Z. Pinwen, Exploring hardness and the distorted sp<sup>2</sup> hybridization of B–B bonds in WB3, *Chem. Mater.* (2014) 5297–5302.
- [47] A.L. Lech, C.L. Turner, R. Mohammadi, S.H. Tolbert, R.B. Kaner, Structure of superhard tungsten tetraboride: a missing link between MB2 and MB12 higher borides, *Proc. Natl. Acad. Sci. U. S. A.* 112 (2015) 3223–3228.
- [48] G. Akopov, M.T. Yeung, C.L. Turner, R. Mohammadi, R.B. Kaner, Extrinsic hardening of superhard tungsten tetraboride alloys with group 4 transition metals, *J. Am. Chem. Soc.* 138 (2016) 5714–5721.
- [49] R. Psiuk, H. Słomińska, J. Hoffman, T. Mościcki, Super-hard films W-B and W-Ti-B deposited from targets sintered by SPS method, *Metal Forming* 30 (2) (2019) 107–120.
- [50] B. Grančič, M. Pleva, M. Mikula, M. Čaplovičová, L. Satrapinskyy, T. Roch, M. Truchlý, M. Sahul, M. Gregor, P. Švec Sr., M. Zahoran, P. Kúš, Stoichiometry, structure and mechanical properties of co-sputtered Ti1-xTaxB2 ±  $\Delta$  coatings, *Surf. Coat. Technol.* 367 (2019) 341–348.
- [51] J.M. Lackner, W. Waldhauser, A. Alamanou, C. Teichert, F. Schmied, L. Major, B. Major, Mechanisms for self-assembling topography formation in low-temperature vacuum deposition of inorganic coatings on polymer surfaces, *Bulletin of the Polish Academy of Sciences Technical Sciences* 58 (2010) 281–294.
- [52] G.L. Humphrey, The heats of formation of TiO, Ti2O3, Ti3O5 and TiO2 from combustion calorimetry, *J. Am. Chem. Soc.* 73 (4) (1951) 1587–1590.
- [53] A.D. Mah, The heats of formation of tungsten trioxide and tungsten dioxide, *J. Am. Chem. Soc.* 81 (7) (1959) 1582–1583.
- [54] P.H. Mayrhofer, C. Mitterer, Self-organized nanocolumnar structure in superhard TiB2 thin films, *Appl. Phys. Lett.* 86 (2005) 131909.
- [55] A. Jain, S.P. Ong, G. Hautier, W. Chen, W.D. Richards, S. Dacek, S. Cholia, D. Gunter, D. Skinner, G. Ceder, K.A. Persson, The materials project: a materials genome approach to accelerating materials innovation, *APL Materials* 1 (2013) 11002.
- [56] J. Musil, Flexible hard nanocomposite coatings, *RSC Adv.* 5 (2015) 60482–60495.
- [57] A.A. Goncharov, Physical processes of the formation of structure and properties, *Phys. Met. Metallogr.* 111 (2011) 314–324.
- [58] J. Musil, Hard nanocomposite coatings: thermal stability, oxidation resistance and toughness, *Surf. Coat. Technol.* 207 (2012) 50–65.
- [59] T. Goto, T. Hirai, ESCA study of amorphous CVD Si3N4-BN composites, *J. Mater. Sci. Lett.* 7 (1988) 548–550.
- [60] G. Mavel, J. Escard, P. Costa, J. Castaing, ESCA surface study of metal borides, *Surf. Sci.* 35 (1973) 109–116.
- [61] O.Y. Khyzhun, Y.V. Zaulychyn, E.A. Zhurakovskiy, Electronic structure of tungsten and molybdenum germanides synthesized at high pressures, *J. Alloys and Compounds* 244 (1996) 107–112.
- [62] C. Sleight, A.P. Pijpers, A. Jaspers, B. Coussens, On the determination of atomic charge via ESCA including application to organometallics, *J. Electron Spectrosc. Relat. Phenom.* 77 (1996) 41–57.
- [63] A.C. Fischer-Cripps, Critical review of analysis and interpretation of

- nanoindentation test data, *Surf. Coat. Technol.* 200 (2006) 4153–4165.
- [64] C.L. Jiang, Z.L. Pei, Y.M. Liu, H. Lei, J. Gong, C. Sun, Determination of the thermal properties of AlB<sub>2</sub>-type WB<sub>2</sub>, *Appl. Surf. Sci.* (2014) 324–330.
- [65] S. Veprek, S. Reiprich, A concept for the design of novel superhard coatings, *Thin Solid Films* 268 (1995) 64–71.
- [66] C. Schmalzried, R. Telle, B. Freitag, W. Mader, Solid state reactions in transition metal diboride-based materials, *Zeitschrift fuer Metallkunde (Materials Research and Advanced Techniques)* 92 (2001) 1197–1202.
- [67] N.S. Patel, J. Menghani, K.B. Pai, M.K. Totlani, Corrosion behavior of Ti<sub>2</sub>N thin films in various corrosive environments, *J. Mater. Environ. Sci.* 1 (2010) 34–43.
- [68] D. Kek Merl, P. Panjan, M. Cekada, M. Macek, The corrosion behavior of Cr-(C,N) PVD hard coatings deposited on various substrates, *Electrochim. Acta* 49 (2004) 1527–1533.